CHEMISTRY OF MATERIALS

ARTICLE

pubs.acs.org/cm

All in the Packaging: Structural and Electronic Effects of Nanoconfinement on Metal Oxide Nanoparticles

Craig Jolley,[†,‡,∥] Vanessa Pool,[‡,§] Yves Idzerda,[‡,§] and Trevor Douglas*[,†,‡]

[†]Department of Chemistry & Biochemistry, [‡]Center for Bio-inspired Nanomaterials, and [§]Department of Physics, Montana State University, Bozeman, Montana 59717, United States

Supporting Information

ABSTRACT: Encapsulation of inorganic nanoparticles within oligomeric protein cages can provide a multivalent approach for the synthesis of biocompatible nanomaterials by combining the nanoparticle-forming catalytic abilities of the cage interior with the biointeractive exterior surface of the cage. Protein cages provide more than simply a passive compartment for nanoparticle formation: protein-templated nanoparticles can exhibit structural and electronic properties that are dramatically different from materials synthesized without protein templating. Mixed Fe/Mn oxides formed under hydrothermal conditions form a structural series ranging from the γ-Fe_2O_3 (maghemite) to the Mn_3O_4 (hausmannite) spinel structure as the Mn fraction is increased from 0 to 100%, while similar materials formed inside of human ferritin transition instead from maghemite to a layered Mn oxide structure similar to chalcophanite. The electronic properties of the protein-templated nanoparticles, as determined from soft X-ray absorption spectroscopy, also differ from those of their protein-free counterparts, in agreement with the structural results. Protein-templated synthesis may provide the opportunity for powerful control over nanomaterial properties through nanoconfinement, but the ultimate physical basis for these effects remains to be determined.

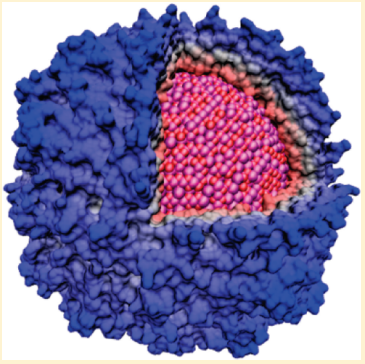

KEYWORDS: composite materials, ferrites, X-ray spectroscopy, pair distribution functions, biomineralization

INTRODUCTION

The formation of hard biomaterials such as mollusk shell or vertebrate bone involves intimate interactions between biopolymers and nascent inorganic crystals.[1−5] Soft materials such as proteins have shown a remarkable capacity to direct the growth and influence the final material properties of hard materials.[6] A growing class of bioinspired nanomaterials[7,8] mimics this formation process by using protein nanocages such as virus capsids[9−12] or ferritins[13−19] to encapsulate inorganic nanoparticles. This approach has a number of immediate advantages for nanotechnology applications: the protein shell can help to prevent aggregation of nanoparticles and can be chemically or genetically modified for in vivo targeting[17,20] or in vitro assembly into hierarchical structures.[21−23]

Another, more subtle effect of protein-confined nanoparticle synthesis is the potential for dramatic changes in the nanoparticle morphology. A simple example is the constraint on crystalline domain size imposed not only by the size of the protein cage but possibly also by the arrangement of crystal nucleation sites on the cage interior.[24] More dramatic effects are also possible: ferritin forms a 24-meric protein cage with interior ferroxidase sites that can oxidize soluble Fe^{2+} to insoluble Fe^{3+}, forming an Fe oxide nanoparticle in the cage interior. Under biologically relevant conditions (room temperature, near-neutral pH, ambient O_2), recombinant ferritin forms a ferrihydrite phase[25] similar to what is observed in native mineralized ferritin. If Fe^{2+} is exposed to the same conditions in the absence of ferritin, however, it precipitates to form a lepidocrocite phase.[26] This can be understood in terms of a kinetic trap: ferritin stabilizes the metastable ferrihydrite phase that transforms into more-ordered Fe oxide structures under most conditions. In fact, such disorder−order transitions in ferritin-templated Fe oxides appear to be feasible only under elevated temperatures requiring the use of ferritins from hyperthermophilic organisms.[19]

Kinetic stabilization of amorphous phases is also relevant to the formation of structural biominerals such as teeth and bones.[3,27] In contrast to classical precipitation models in which growing crystals form directly from the addition of solution ions, calcium phosphate and carbonate have been shown to exist as stable nanometer-sized clusters in solution.[28] Amorphous phases form by aggregation of these nanoclusters, and macroscopically ordered crystals can arise through interaction with an ordered template that establishes crystal phase and orientation.[29] In the case of collagen biomineralization,[3] the amorphous precursor phases are thought to be stabilized by noncollagenous proteins (NCPs), forming negatively charged clusters that are subsequently oriented on the positively charged collagen scaffold and reorganize into a larger-scale crystal. Similar solution-phase molecular clusters have been characterized for transition metals,[30] and ferritin (which also carries a significant

Received: May 6, 2011
Revised: July 17, 2011
Published: August 09, 2011

negative charge) may function similarly to NCPs by electrostatically stabilizing thermodynamically unfavorable amorphous phases. It should be noted, however, that Fe^{2+} ions must enter ferritin through narrow pores at the 3-fold symmetry axes,[31] and it is unlikely that nanometer-scale Fe oxide clusters could pass into the ferritin cage intact: any solution-phase clusters that serve as a precursor to ferrihydrite formation must form inside the cage.

This study focuses on a more synthetically motivated model system: the formation of Mn ferrites (mixed spinels of Fe and Mn) both in a protein-free solution and inside of recombinant human ferritin (HFn). Ferrite spinel nanoparticles have been a subject of intense interest because of their superparamagnetic properties,[32,33] which make them attractive targets for applications including ferrofluids, magnetocaloric refrigeration, and magnetic resonance imaging.[34] In addition, Mn oxides have been shown to form highly porous nanostructures with architectures reminiscent of biological materials,[35] which may be useful in sensing or catalytic applications that require high surface area. HFn has previously been shown to grow nanoparticles of γ-Fe_2O_3 under conditions of controlled oxidation at elevated pH and temperature; these particles show a strong magnetic response and are being investigated as potential contrast agents for magnetic resonance imaging.[17,20,36] When HFn is incubated with Mn^{2+} under similar conditions, Mn oxide nanoparticles form instead; mixed Fe/Mn oxides grown in HFn have previously been studied using L_{23}-edge X-ray absorption spectroscopy (XAS).[37]

When structural information obtained from X-ray pair distribution function (PDF) analysis is integrated with electronic information from L_{23}-edge XAS, it becomes clear that the protein template exerts a profound influence on the properties of the encapsulated metal oxide nanoparticle. The implications of this finding are both daunting and promising: daunting because the mechanistic details of a protein template's influence on nanoparticle formation are so poorly understood, and promising because the mere existence of such dramatic effects suggests that protein templates can be engineered for the formation of application-oriented materials with specific novel properties.

MATERIALS AND METHODS

Protein Expression and Purification. Recombinant HFn was obtained by overexpression in *Escherichia coli* BL21 cells as described previously.[17,36] All protein-based samples were purified by size exclusion chromatography (SEC) and subsequent anion exchange chromatography before mineralization.

Synthesis. Mn ferrite samples were synthesized at doping levels ranging from 0 to 100% Mn. Solutions of 12.5 mM $(NH_4)_2Fe(SO_4)_2 \cdot 6H_2O$ and 12.5 mM $MnCl_2$ were prepared using H_2O that had been sparged with N_2 to remove dissolved oxygen and mixed to obtain the desired $[Fe^{2+}]/[Mn^{2+}]$ ratio. A syringe pump (KD Scientific) was used to simultaneously add the 12.5 mM metal mixture and a deaerated 4.17 mM H_2O_2 solution to a stirred reaction vessel. The reaction vessel temperature was maintained at 65 °C using a heated water bath (VWR) and the pH maintained at 8.5 by addition of deaerated 100 mM NaOH using an autotitrator (718 STAT Titrino, Metrohm). The reaction vessel initially contained a deaerated solution of 100 mM NaCl, to ensure proper functioning of the pH electrode. For protein-templated samples, purified HFn in unbuffered 100 mM NaCl was added to the reaction vessel at a concentration of ~0.3−0.5 mg/mL prior to mineralization. The metal ion and H_2O_2 solutions were added at a rate of 40 mL/h, and solutions were kept under a nitrogen atmosphere throughout synthesis. The same temperature and pH conditions were used in the protein-free and protein-templated reactions. Nanoparticle confinement inside the protein cages was confirmed using size-exclusion chromatography, dynamic light scattering, and transmission electron microscopy (TEM), as described elsewhere.[17,24,36] The protein-free reaction solution was turbid and nearly black for 100% Fe, shading to a lighter brown for 100% Mn. For samples with <50% Mn, ferromagnetism was visually confirmed using a small magnet. When HFn was included, the reaction solutions showed similar color changes but were clear and lacked visible magnetic response.

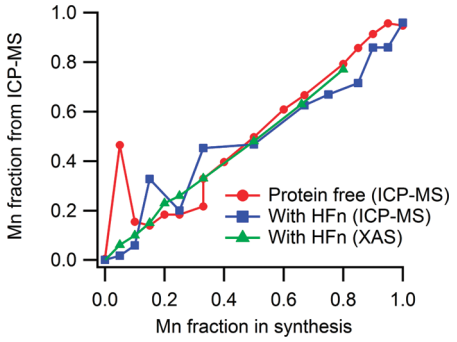

Figure 1. Mn doping levels determined by ICP-MS and by comparing the Mn and Fe XAS integrated intensities. Measured Mn fractions correlate well with the Mn^{2+}/Fe^{2+} ratios used during synthesis, indicating a lack of systematic bias in Mn^{2+} uptake by HFn or incorporation into the growing nanoparticle relative to Fe^{2+}.

Protein-free samples were centrifuged and washed 3× with deionized water to remove NaCl and unreacted metal ions. Protein-templated samples were purified by SEC with a running buffer of 50 mM PO_4^-, 100 mM NaCl, pH 7.5; samples intended for PDF analysis were then dialyzed for ~7 days against several changes of ddH_2O to remove unwanted electrolytes. Samples to be used for XAS measurements were stored in an aqueous suspension, while samples to be used for PDF analysis were dried to powder using a vacuum lyophilizer (FreeZone, Labconco).

Electronic Structure Determination. The Fe and Mn L_{23}-edge XAS and X-ray magnetic circular dichroism (XMCD) were measured at beamlines 6.3.1 and 4.0.2 of the Advanced Light Source at the Lawrence Berkeley National Laboratories. The samples were dried in air on Formvar-coated TEM grids prior to introduction into the ultrahigh vacuum chamber. The XAS measurements were made at room temperature using linearly polarized light in both total electron yield mode, in which the current required to replenish photoelectrons ejected from the sample is monitored, and in transmission mode using a Ga photodetector. Although both collection methodologies produced the same results, the electron yield had a lower noise level and is reported here. The incident photon flux was determined from an 80% transmission gold grid upstream from the sample. The XMCD measurements[38] were made in the presence of a ± 1.5 T magnetic field with 90% circular polarized light. All reported XMCD spectra are corrected for incomplete polarization. Energy referencing was accomplished using an internal reference powder mix (Fe_3O_4 and MnO) where the major peak in the Fe and Mn L_3-edges have been set to be 704.70 and 637.75 eV, respectively.

Pair Distribution Function (PDF) Analysis. Pair distribution functions of the Mn ferrite samples were determined by high-energy total X-ray scattering. Powdered samples were placed in cylindrical Kapton capillaries with inner diameter 0.0575″ (Cole-Parmer) and X-ray scattering was collected at a wavelength of 0.2128 Å on beamline 11-ID-B at the Advanced Photon Source at Argonne National Laboratories. Powder diffraction patterns were assembled by averaging 0.5 s

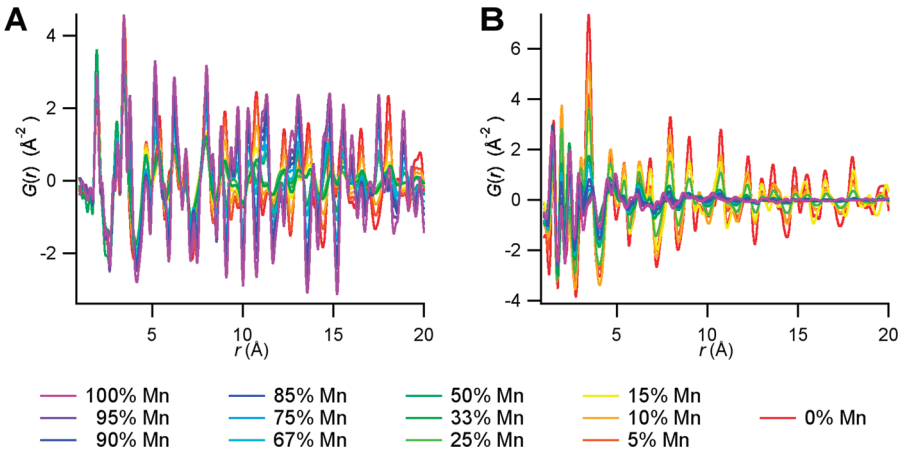

Figure 2. Experimentally determined PDFs for Mn doping series under protein-free (A) and protein-templated (B) conditions. Note the general agreement at short distances (especially <4 Å) and the larger divergence at longer distances (>8 Å), indicating the presence of two distinct structural types.

exposures, with a total collection time of 5 min for each sample; diffraction image processing used the Fit2D software package.[39] Diffraction patterns were radially integrated to obtain a one-dimensional trace of the total scattering; data up to q = 19.2 Å^{-1} for protein-templated samples and q = 23.0 Å^{-1} for protein-free samples were used to obtain the corrected X-ray structure factor $S(q)$. The radial pair distribution function $G(r)$ was obtained via a Fourier transform of $S(q)$; calculation of $S(q)$ and $G(r)$ used the PDFGetX2 software package.[40] Unit cell structures for bulk materials were obtained from the MINCRYST web server,[41] and the PDFgui software package[42] was used to fit crystal models to the experimental $G(r)$.

Compositional Analysis. Relative concentrations of Mn and Fe were measured for all samples using inductively coupled plasma mass spectrometry (ICP-MS) and by comparing peak edge jumps in the Fe and Mn XAS spectra after referencing to a Fe_2MnO_4 reference powder. Measured Mn/Fe ratios were roughly equal to the ratios used during synthesis (Figure 1) and do not indicate any systematic compositional bias in Mn ferrite mineralization, either in HFn or in protein-free solution.

RESULTS

Radial Pair Distribution Function *G*(*r*) Shows Dramatic Structural Changes with Mn Doping. The experimentally determined $G(r)$ for Mn ferrites with and without protein are shown in Figure 2. For the protein-free samples, $G(r)$ shows a range of shapes with two end point structures represented by γ-Fe_2O_3 (maghemite) and Mn_3O_4 (hausmannite). The plotted curves show general agreement at short distances (r < 8 Å), indicating that the spinel structure shared by both maghemite and hausmannite is present in all of the samples and that their local geometries are similar. At larger distances, the structures observed are dramatically out of register with each other (note the alternating peaks for r > 9 Å), suggesting that there is a change in unit cell spacing between the two structural types. The changes in the protein-templated samples are even more dramatic, with the high-Fe samples showing a spinel structure and the high-Mn samples appearing largely amorphous, with virtually no $G(r)$ features beyond ~7 Å.

Note that $G(r)$ tapers off with increasing r, and that this tapering effect is more pronounced in some samples than in others; this is a result of the finite size of crystalline domains.[43] The amplitude of $G(r)$ decreases once r becomes comparable to the crystalline domain size because fewer such long-range correlations can be found. In our data fitting protocol, this effect is modeled by assuming spherical domains and convoluting the modeled $G(r)$ by a spherical shape factor. The diameter of the assumed spherical domains is a parameter that can be fit to the data to obtain a typical domain size.

Fitting of Protein-Free Structures. To determine the nature of the structural changes that occur in the protein-free samples upon changing the Fe/Mn ratio in the synthesis, the doped samples were fit using the crystal structures of bulk maghemite (γ-Fe_2O_3) and hausmannite (Mn_3O_4). Maghemite and magnetite (Fe_3O_4) give virtually identical X-ray PDFs; usage of a Fe_3O_4 model rather than a γ-Fe_2O_3 model in the fitting procedures below produced negligibly different results. While Fe XAS spectra have been used to differentiate between various Fe oxides,[44] our XAS measurements (see below) also did not provide adequate information to distinguish γ-Fe_2O_3 from Fe_3O_4. The structure will be referred to below as γ-Fe_2O_3 with the understanding that this designation is not entirely conclusive.

Three different fitting schemes were employed. The first assumes a simple mixture of phases: fits were performed for the γ-Fe_2O_3 and Mn_3O_4 phases, and the doped phases were assumed to be simple mixtures of these phases. The γ-Fe_2O_3 sample was well-described by maghemite with a crystalline domain size of 5.2 nm, while Mn_3O_4 was well-described by hausmannite with a somewhat larger domain size of 14.7 nm (Figure 3A,B). Mixtures of these two phases, however, did not provide an adequate description of the doped samples (Figure 3C); in general, the two-phase models gave higher amplitudes at large r than were observed experimentally, indicating that a model based on a simple two-phase mixture overestimates the crystallinity of the doped samples.

In the second fitting scheme attempted (Figure 4), the doped samples were assumed to consist of a mixture of the two bulk crystal phases, but the spherical domain diameter was treated as a free variable that was fit separately for each doped sample. Two things are immediately apparent from this fitting procedure. The first is that, while the pure γ-Fe_2O_3 and Mn_3O_4 samples are well-described by the bulk crystal structures, the fraction of Mn_3O_4 used to fit the experimental $G(r)$ is a monotonically increasing function of Mn concentration, as would be expected. Second, one

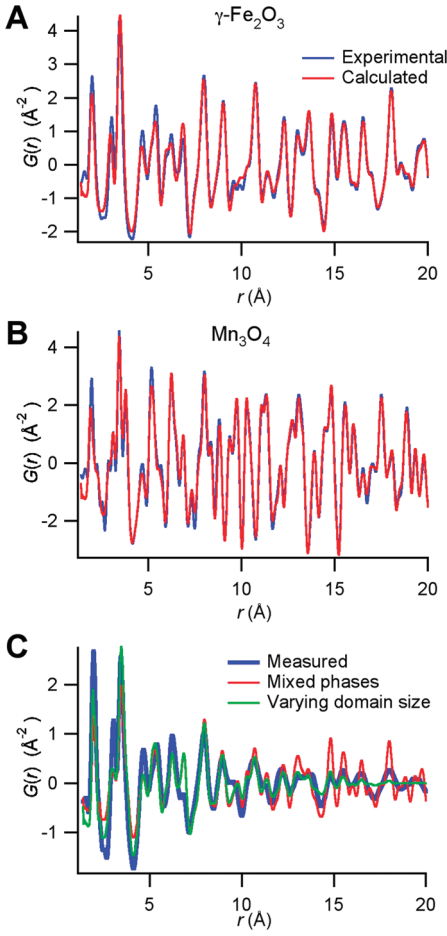

Figure 3. Experimental $G(r)$ and model fits for protein-free γ-Fe_2O_3 (A), Mn_3O_4 (B). γ-Fe_2O_3 doped with 25% Mn (C) was fit using the fitting schemes described in the text. Note that a simple mixture of the γ-Fe_2O_3 and Mn_3O_4 phases without a reduction in the crystalline domain size (red trace, see Figure 4A) results in an overestimation of the $G(r)$ amplitude at high r. Allowing the domain size to fluctuate along with the γ-Fe_2O_3/Mn_3O_4 composition (green trace) results in an improved fit. Several differences still persist, notably the dramatic overestimation of a peak height at ~7 Å; these may result from defects or other deviations from the idealized spinel model.

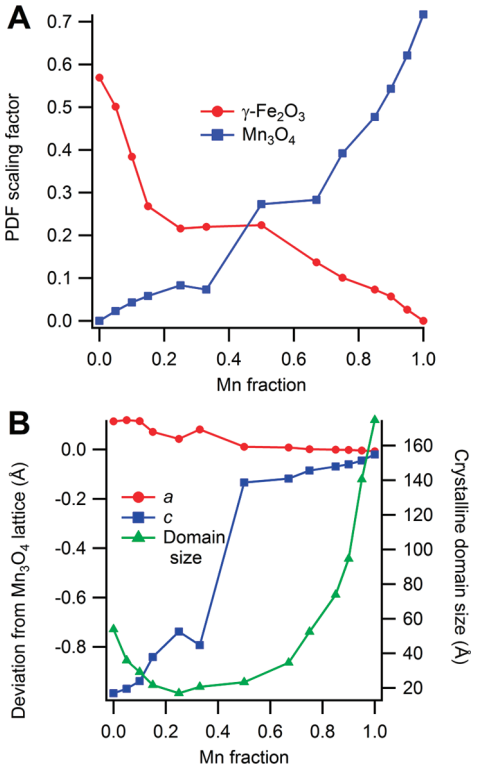

Figure 4. (A) Relative ratios of Fe_3O_4 and Mn_3O_4 as a function of Mn doping, in the two-phase fit model. (B) Crystalline domain size and lattice parameter changes as a function of Mn doping. The pure Fe_3O_4 and Mn_3O_4 samples are more crystalline (i.e., have larger domain sizes), while the domain size shrinks dramatically in the samples with intermediate doping levels. As Mn concentrations increase, the unit cell elongates along the c axis and contracts slightly along the two perpendicular ($a = b$) axes.

can see the reason for the failure to fit the correct particle size in the two-phase approach; there is a dramatic loss of crystallinity at intermediate doping levels, with the crystalline domain size shrinking to as little as 2 nm in the case of 25% Mn.

The final fitting approach made use of the fact that the γ-Fe_2O_3 data can be fit reasonably well with the bulk hausmannite model, as long as the unit cell parameters are allowed to vary. The opposite approach was not as successful, probably because the cubic structure of γ-Fe_2O_3 does not allow for the anisotropic lattice distortions required to fit Mn_3O_4 properly. All samples could be fit with a single crystal phase, and the free parameters that varied from one sample to another were the crystalline domain size and the axis lengths a and c of the orthorhombic unit cell. (Figure 4). As Mn content increases from 0 to 33%, there is a slow increase in c. Between 33% and 50% Mn, c increases dramatically, and then settles into another slow increase in the region from 50% to 100% Mn. Between 0 and 100% Mn, c undergoes an overall increase of about 1 Å. At the same time, we see a much smaller decrease in a which appears to lack the same type of sudden change. Comparison of Figures 4A and 4B shows that the sharp increase in c happens at the same Mn fraction as a similar, but less distinct, increase in the Mn_3O_4 contribution to the mixed model. This point, somewhere between 33% and 50% Mn, can be identified as the doping level at which a transition between a maghemite-like lattice and a hausmannite-like lattice takes place.

Two major conclusions can be drawn from these model-fitting results. The first is that a major structural change occurs at a Mn doping level of between 33 and 50%. The clearest way to interpret this is using Figure 4B, which shows a dramatic increase in the length of the unit cell c axis, corresponding to a sudden change from a γ-Fe_2O_3-like lattice to a Mn_3O_4-like lattice (Figure 4A). The other major result is that both end points of the doping series show comparatively high crystallinity (Figure 4B), while intermediate doping values are far less crystalline. The minimum crystalline domain size is reached at doping levels fairly close to the abrupt increase in the unit cell c axis, possibly indicating that local compositional heterogeneities lead to structural defects which inhibit the formation of large crystalline domains.

Fitting of Protein-Templated Structures. HFn-templated γ-Fe_2O_3 samples have previously been characterized by PDF analysis[24] and show excellent fits to maghemite (or, equivalently, magnetite) structures. This spinel-like structure was present without any major changes from 0 to 25% Mn (Figure 2). After

dx.doi.org/10.1021/cm201295p |Chem. Mater. 2011, 23, 3921–3929

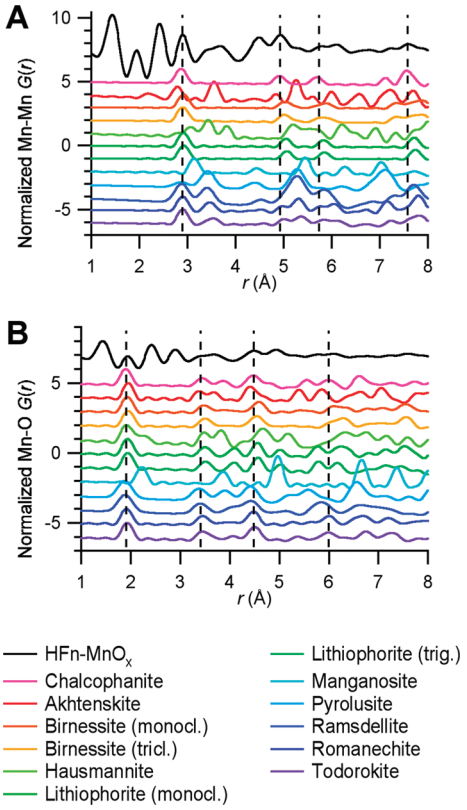

Figure 5. Comparison of HFn-templated 100% Mn oxide with calculated PDFs of known Mn oxide phases. When only Mn−Mn correlations are plotted (A), it is clear that the edge-sharing MnO_6 peak at 2.9 Å is clearly present in the experimental data, while the vertex-sharing MnO_6 peak at 3.5 Å that is present in many Mn oxide phases is lacking in the experimental data. The peak at around 4.9 Å agrees well with an Mn−Mn correlation in chalcophanite; the corresponding distances in the other phases are all too long. Plotting the Mn−O correlations (B), allows us to clearly identify the Mn−O bond correlation at 1.9 Å, along with features at 3.4 and 4.4 Å arising from edge-sharing MnO_6 octahedra.

this point, however, things change dramatically. The measured PDFs for high-Mn samples did not provide a satisfactory fit to hausmannite, or to other pure Mn-oxide phases (akhtenskite, manganosite, pyrolusite, ramsdellite). Taking a cue from PDF studies of biogenic Mn oxides formed by bacteria and fungi,[45] we attempted to fit to a variety of weakly ordered Mn oxide phases (lithiophorite, birnessite, romanechite, todorokite, and chalcophanite), which often contain H_2O and well-ordered counterions (mostly Group 1 and 2 ions, along with Al^{3+} in lithiophorite and Zn^{2+} in chalcophanite) in the crystal structure.

The 100% Mn oxide sample in HFn shows several clear features at low r that can aid in phase identification (Figure 5). First, there are the clear peaks at 1.5 Å and 2.5 Å that are observed in all protein-templated nanoparticle PDFs[12,24] and arise from correlations between bonded carbon and nitrogen atoms (1.5 Å) and second-nearest neighbors (2.5 Å) in protein. Other low-r peaks are diagnostic for Mn oxide phases; a peak at about 1.9 Å has decreased amplitude because of its position in the valley between the major protein peaks, but agrees well with distances measured for Mn−O bonds. A correlation at 2.9 Å arises from Mn−Mn correlations in edge-sharing MnO_6 octahedra; the asymmetric feature at 3.7 Å is somewhat longer than Mn−Mn correlations in vertex-sharing MnO_6 octahedra but matches well

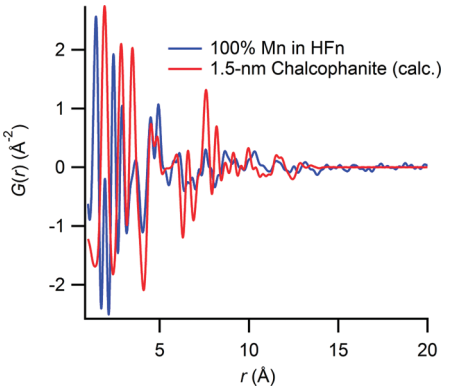

Figure 6. Measured PDF for 100% Mn oxide in HFn, compared with a calculated PDF for chalcophanite with a 1.5 nm spherical domain size. The protein peaks at ∼1.5 and ∼2.5 Å are absent in the calculated structure, and several of the peaks are lower-amplitude in the protein structure, reflecting the presence of defects. The prominent set of peaks at 7−8 Å in the calculated PDF results from correlations between planes of MnO_6 octahedra; their lower amplitude in the measured PDF reflects interplane stacking faults that render the idealized model of spherical crystal domains unreliable.

with a Mn−O peak for second-nearest neighbors. Many structures with edge-sharing MnO_6 show a Mn−O correlation near 4.5 Å that agrees well with the experimental peak observed at 4.4 Å; beyond this distance the differences between different phases begin to look more dramatic. Most significantly, many phases show a significant Mn−Mn correlation near 5.3 Å; most of these are longer than the 4.9 Å peak observed experimentally, but the peak for chalcophanite is quite close. An overlay of the experimental PDF and a calculated PDF for chalcophanite with a domain size of 15 Å is shown in Figure 6; note that the double peak at around 6 Å is also fairly well duplicated.

The calculated chalcophanite structure contains features at ∼7.5 Å which arise from interlayer Mn−Mn correlations; these are largely absent in the measured PDFs and indicate that interlayer stacking faults are present in the protein-templated samples, leading to weak overall order. The crystalline domain model used for PDF calculations in PDFgui assumes spherical domains which are unlikely to be an accurate approximation in such an anisotropic structure. Interestingly, biogenic Mn oxides produced by bacteria fit to a birnessite-like layered structure that is similar to chalcophanite, in contrast to fungal Mn oxides which fit to a tunnel-like todorokite structure; it remains unclear whether the mechanistic details of bacterial chalcophanite formation might be similar to what was observed in our experiments.

Previous work[24] has identified the Mn oxide phase synthesized in HFn under the reaction conditions described as a hausmannite structure, similar to what was observed in the protein-free case. While the synthesis conditions described in this study are essentially identical to those in these previous studies, the postsynthesis size-exclusion chromatography (SEC) purification step was absent. Given the largely amorphous structure of protein-templated Mn oxides and the highly crystalline structure of the protein-free samples, it is possible that a small amount of bulk crystallization (which would be removed by SEC) could give a spurious hausmannite diffraction pattern. The fact that nearly identical PDFs were obtained for a variety of high-Mn

dx.doi.org/10.1021/cm201295p |*Chem. Mater.* 2011, 23, 3921–3929

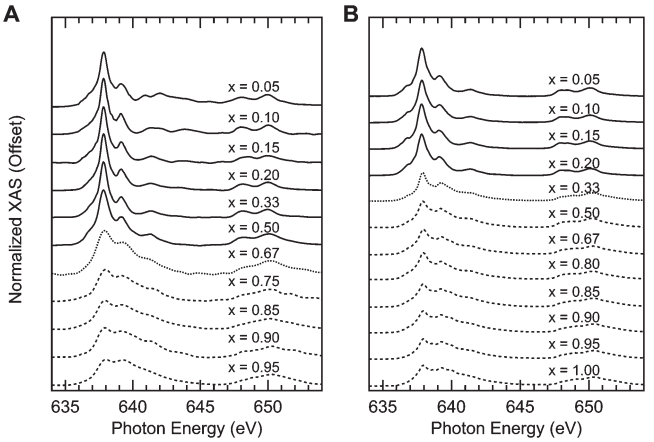

Figure 7. Area normalized Mn L_{23}-edge XAS spectra for particles with protein (left panel) and without protein (right panel). Line types indicate similar phases (solid line is low Mn concentration phase, dashed line is high Mn concentration, and dotted line is transition region).

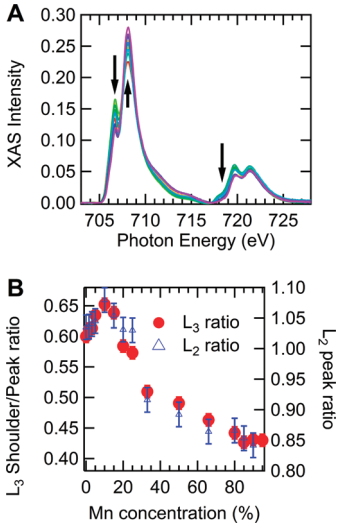

Figure 8. (A) Area normalized Fe L_{23}-edge XAS spectra for particles without protein. The color range for Mn doping levels is the same as in Figure 1. Arrows indicate the evolution trend of various features as the Mn concentration is increased. (B) Ratio of the intensities of the L_3 shoulder feature (706.5 eV) and main L_3 peak (708 eV) displayed as solid circle using left axis and the intensity ratio of the first L_2 peak (719.5 eV) and second L_2 peak (721.5 eV) displayed as open triangles using right axis.

doping levels suggests that the results presented here probably do not stem from an error in synthesis or characterization, but that the structure of protein-templated Mn oxide nanoparticles (which have been rigorously purified) is not highly crystalline.

Electronic Properties. The Mn L_{23}-edge XAS spectra for a representative sampling of different Mn concentrations with and without protein are shown in Figure 7. The spectra have been normalized to the integrated peak area (L_2+L_3) and energy calibrated by comparing the peak position of a reference powder that is simultaneously collected with each sample spectra. The evolution of the spectra for the protein-free particles (right panel) shows that as the Mn concentration is reduced, the Mn L_{23} spectral weight shifts dramatically from the higher-energy peaks to the lower-energy peak. The spectra are quite similar for

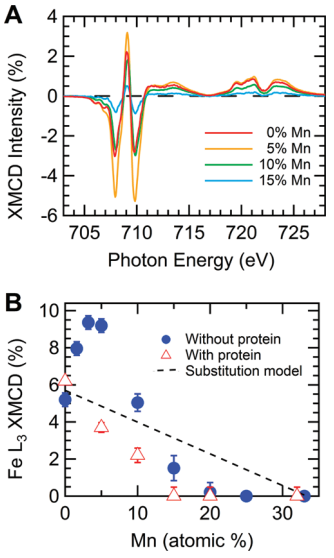

Figure 9. (A) Fe L_{23}-edge XMCD spectra for particles without protein for different Mn concentrations. (B) The Fe peak-to-peak MCD variation with Mn concentration without protein (solid circles), with protein (open triangles), and a calculated linear moment reduction for Mn displacement of Fe in the octahedral site (dashed line).

5%−25% Mn concentrations, changing rapidly at 33% Mn. Above this concentration, the Mn spectra evolve gradually, but are all quite similar. The range of Mn concentrations over which the electronic structure evolves rapidly is the same range at which dramatic structural changes were observed (see above).

While the overall trend in the Mn L_{23}-edge XAS of the protein-templated particles (left panel) is fairly similar to the protein-free particles, important differences exist. In particular, the highly structured peaks seen at low Mn concentrations persist to higher Mn doping levels in the protein-templated samples, changing suddenly after 67% Mn instead of 33% Mn. Above 75% Mn, the electronic structure remains fixed. There are also subtle differences in the shapes of both the high-Mn and low-Mn spectra.

Confirmation of this varied evolution of the structure of Mn ferrite nanoparticles can be found in the Fe XAS spectra. Figure 8A displays the area normalized Fe L_{23}-edge XAS spectra for protein-free nanoparticles. The slight change in the local electronic structure of Fe is conveyed in the changing shoulder intensity of the L_3 peak in comparison to the main peak and in the redistribution of spectral weight between the first and second peak of the L_2 edge (along with the development of a small shoulder at lower binding energy). These variations are qualitatively clear from the spectra themselves, but the trend can be quantitatively understood by displaying these two intensity ratios (Figure 8B). Once again we see a gradual evolution of the Fe electronic spectra from 0%−33% Mn, with a transition around 50% Mn. These changing ratios have been attributed to increased occupation of Fe in the octahedral site of the spinel structure, consistent with the Mn displacing Fe in the tetrahedral site. The corresponding Fe L_{23}-edge spectra for the protein-templated particles are very similar to those published previously and are included in the Supporting Information accompanying this article.

Additional structural information can be obtained from the XMCD spectra of the L_{23} edge.[46] Figure 9 shows the evolution of the Fe XMCD as a function of Mn concentration for protein-free

dx.doi.org/10.1021/cm201295p |*Chem. Mater.* 2011, 23, 3921–3929

particles. The spectra show that the dichroism signal of Fe first dramatically increases at low Mn addition, then falls rapidly. This behavior, highlighted by the solid circles in Figure 9B, is well understood if the Mn initially substitutes for Fe in the A-site (tetrahedral) position. In the spinel structure, because of indirect exchange coupling, the magnetic orientation of the Fe in the A-site is opposite the magnetic orientation of Fe in the more numerous octahedral B-sites, resulting in a reduction of the net Fe moment. Substitution of Mn into the A-site reduces the occupation of Fe in this site, thus increasing the net Fe moment. Also shown in the Figure 9B (dashed line) is the calculated Fe MCD signal if the Mn were to merely displace the Fe atoms from the octahedral site. In contrast, for Mn addition with protein encapsulation, the Fe MCD signal is observed to drop rapidly to zero and is consistent with Mn substituting as Mn^{2+} in the octahedral B-site, displacing the Fe and reducing the overall moment.[37] Moreover, both the Fe L_3 XMCD line shape and the Mn L_3 XAS line shape show that as the Mn concentration increases, the fraction of Fe atoms with an Fe^{3+} valence in the octahedral site decreases while the occupation of the octahedral site by Mn increases.[47] For both the protein-free (solid circles) and protein-templated samples (open triangles), the eventual decrease in the net Fe moment is significantly faster than the hypothetical linear decrease. This suggests that Mn does more than simply dilute the magnetism of the Fe atoms; significant levels of Mn disrupt the magnetic coupling, effectively abolishing ferromagnetic behavior by 25% Mn incorporation.

DISCUSSION

Agreement of PDF and XAS Methods. The results obtained by PDF analysis and L-edge XAS studies of these materials are in broad agreement, and the data obtained by these two methods are largely complementary. As a diffraction method, PDF analysis is highly sensitive to small shifts in the unit cell geometry. For example, the Mn ferrites shown in Figure 2A look extremely similar at very short distances (<4 Å); it is only at higher values of r that the changes in the lattice geometry resulting from the substitution of Mn for Fe become apparent. For these oxide materials, the XAS is a much more local method, revealing information only about the immediate coordination environment of the element whose absorption edge is being measured. Comparison of Figure 2 with Figure 7, for example, indicates that, although the protein-templated and protein-free Mn oxide nanoparticles show dramatically different crystal structures (chalcophanite-like and hausmannite-like, respectively), the coordination environments of the Mn atoms are fairly similar. In both cases, the Mn X-ray absorption signal is dominated by distorted MnO_6 octahedra, in contrast to the less-distorted structures that prevail when Mn is doped into a lattice dominated by Fe oxide. PDF analysis struggles to extract information from very weakly ordered materials (such as the protein-templated Mn oxides), while XAS spectra are less sensitive to the degree of larger-scale order.

Valence and Site Occupation of Mn Atoms. This combined PDF/XAS approach is particularly fruitful in determining the incorporation of Mn into the γ-Fe_2O_3 lattice at low Mn concentrations. Figure 7 shows that the two types of samples undergo roughly similar changes, from well-defined spectra indicative of relatively undistorted Mn geometries to broader spectra that suggest the distorted geometries present in many bulk Mn oxides. These changes happen, however, at rather different concentrations: around 33% Mn in the protein-free samples and around 67% in the protein-templated samples. If Mn were incorporating preferentially into the tetrahedral A-sites of the spinel lattice, one would expect a transition at about 33% doping, when all of these sites became occupied. Conversely, a transition at around 67% occupancy would suggest incorporation into the octahedral B-sites. Further evidence can be gleaned from the shape of the XAS spectra themselves; the low-concentration (5% Mn) spectrum of the protein-free nanoparticles is nearly identical to the theoretical spectrum of Mn^{2+} in a tetrahedral configuration,[48] consistent with incorporation into the A-sites. In the Fe XMCD results (Figure 9), the initial substitution of Mn into the ferromagnetic A-sites serves to increase the net Fe moment, at least until Mn concentrations become high enough to interfere with the long-range magnetic coupling of the Fe sites. In contrast, the protein-templated nanoparticles show no such increase, suggesting that they do not prefer the A-sites at low doping levels.

The PDF results paint a similar picture for the protein-free nanoparticles; Figure 4 shows a dramatic change in the spinel lattice parameters at around 33% Mn, consistent with the XAS results indicating initial doping into the tetrahedral sites. The protein-templated particles are somewhat different; close examination of Figure 2 suggests that the spinel structure has largely broken down by 33% Mn, being replaced by the layered chalcophanite-like structure, in which all metal sites are octahedral. Because of the overall weak ordering of this phase, it is impossible to determine what subtle structural shifts may be taking place at higher Mn doping levels. The XAS spectra reported in Figure 7 suggest that, in the 33−67% Mn range, the character of this weakly ordered lattice is still sufficiently determined by Fe as to create largely undistorted local environments for the Mn ions. It is only at doping levels above about 67% that the distorted Mn octahedral geometries become clearly apparent.

Loss of Crystallinity at Intermediate Doping in Samples. As an increasing number of Mn atoms are inserted into the γ-Fe_2O_3 lattice (or conversely, Fe atoms into Mn_3O_4), they will introduce defects that will tend to decrease the crystalline domain size in the material. A simple calculation indicates, however, that the spinel lattices are fairly tolerant of Fe/Mn substitutions. For example, γ-Fe_2O_3 has a molar volume of 43.71 cm^3/mol; this corresponds to about 2.8×10^{22} Fe/cm^3, or a characteristic inter-Fe spacing of roughly 3.3 Å. If 5% of these Fe atoms are replaced with Mn and each Mn substitution is a defect site, then the Mn density will be 1.4×10^{21} Mn/cm^3, for an inter-Mn spacing of about 9 Å. The crystalline domain size at 95% Fe is nearly 36 Å, meaning that (in this rough approximation) a defect is introduced at 0.08% of Fe lattice sites, or 1.6% of Mn substitution sites. It is more likely that isolated Mn atoms can be incorporated into the Fe oxide lattice fairly easily (and vice versa) while a cluster of several nearby Mn atoms will be sufficient to introduce a defect.

Spinel-Chalcophanite Transition. In the high-Mn protein-templated samples, crystallinity loss likely involves a different mechanism, as the nanoparticle adopts a chalcophanite-type lattice that is dramatically different from the spinel lattice present in the high-Fe samples; the reasons for this structural change are less clear. In the protein-free synthesis, the 100% Mn samples showed larger domain sizes than the 100% Fe samples (Figure 4); it is possible that the tightly bonded hausmannite structure is only stable in fairly large, well-ordered crystalline

domains, while the layered chalcophanite structure can easily be disrupted by defects and is more amenable to a nanoconfined environment. By analogy with the protein-directed formation of calcium phosphate biominerals,[3] it is possible that ferritin affects the crystal phase of Mn-dominated oxide phases either through electrostatic stabilization of thermodynamically unfavorable amorphous phases or by limiting nucleation precursors to individual ions which can successfully enter the protein cage, rather than nanometer-scale metal oxide clusters. The possible role of cage entry is highlighted by the fact that Fe oxide phases can easily be formed within both human ferritin (used in this study) and ferritin from the hyperthermophilic Archaeon *Pyrococcus furiosus*,[49] while attempts to form Mn oxide nanoparticles within *Pyrococcus* ferritin were unsuccessful. This suggests that the kinetics of cage entry may be affected by subtle details of the protein cage structure, leading to a significant impact on nanoparticle formation.

CONCLUSION

Protein cages used for inorganic nanoparticle encapsulation are far more than just passive containers; they exert a significant influence on the structural and electronic properties of the composite nanomaterials. Pair distribution function analysis from total X-ray scattering clearly shows that the structural changes experienced by Mn ferrite nanoparticles as a function of increasing Mn doping is qualitatively different in HFn-templated and protein-free nanoparticles. The reasons for this difference are not as clear: possibilities include changes in lattice stability because of the small crystalline domain size enforced by protein cage confinement and multiple nucleation sites or kinetic effects on crystal growth resulting from the limited rate of ion diffusion into the cage. A more thorough understanding of the physical underpinnings of these cage-induced material effects will be essential to realize the full potential of protein-mediated inorganic nanomaterials synthesis.

ASSOCIATED CONTENT

Supporting Information. Further details are given in Figures S1 and S2. This material is available free of charge via the Internet at http://pubs.acs.org.

AUTHOR INFORMATION

Corresponding Author

*E-mail: tdouglas@chemistry.montana.edu.

Present Addresses

[||]Laboratory for Systems Biology, RIKEN Center for Developmental Biology, Kobe, Japan.

ACKNOWLEDGMENT

This research was supported in part by grants from the U.S. Department of Energy, Office of Basic Energy Sciences, Division of Materials Science and Engineering DE-FG02-07ER46477, the National Science Foundation under Grant CBET-0709358, and the NASA Astrobiology Institute (NNA08CN85A). Compositional analysis by ICP-MS was carried out by Energy Laboratories, Inc., Billings, MT. X-ray scattering was obtained at beamline 11-ID-B at the APS with the assistance of Karena Chapman, Peter Chupas, and Evan Maxey. The Advanced Photon Source is supported by the U.S. Department of Energy under Contract No. DE-AC02-06CH11357. The Advanced Light Source is supported by the U.S. Department of Energy under Contract No. DE-AC02-05CH11231.

REFERENCES

(1) Belcher, A. M.; Hansma, P. K.; Stucky, G. D.; Morse, D. E. *Acta Mater.* **1998**, *46* (3), 733–736.
(2) Weiner, S.; Wagner, H. D. *Annu. Rev. Mater. Sci.* **1998**, *28*, 271–298.
(3) Nudelman, F.; Pieterse, K.; George, A.; Bomans, P. H. H.; Friedrich, H.; Brylka, L. J.; Hilbers, P. A. J.; de With, G.; Sommerdijk, N. A. J. M. *Nat. Mater.* **2010**, *9* (12), 1004–1009.
(4) Kröger, N.; Deutzmann, R.; Sumper, M. *Science* **1999**, *286* (5442), 1129–1132.
(5) Kröger, N.; Deutzmann, R.; Bergsdorf, C.; Sumper, M. *Proc. Natl. Acad. Sci. U. S. A.* **2000**, *97* (26), 14133–14138.
(6) Klem, M. T.; Willits, D.; Solis, D. J.; Belcher, A. M.; Young, M.; Douglas, T. *Adv. Funct. Mater.* **2005**, *15* (9), 1489–1494.
(7) Dujardin, E.; Mann, S. *Adv. Mater.* **2002**, *14* (11), 775–788.
(8) Aizenberg, J. *Adv. Mater.* **2004**, *16* (15), 1295–1302.
(9) Douglas, T.; Young, M. *Nature* **1998**, *393* (6681), 152–155.
(10) Douglas, T.; Young, M. *Science* **2006**, *312* (5775), 873–875.
(11) Young, M.; Willits, D.; Uchida, M.; Douglas, T. *Annu. Rev. Phytopathol.* **2008**, *46*, 361–384.
(12) Jolley, C. C.; Klem, M. T.; Harrington, R.; Parise, J. B.; Douglas, T. *Nanoscale* **2011**, *3*, 1004–1007.
(13) Douglas, T.; Dickson, D. P.; Betteridge, S.; Charnock, J.; Garner, C. D.; Mann, S. *Science* **1995**, *269* (5220), 54–57.
(14) Meldrum, F. C.; Douglas, T.; Levi, S.; Arosio, P.; Mann, S. *J. Inorg. Biochem.* **1995**, *58* (1), 59–68.
(15) Wong, K. K. W.; Mann, S. *Adv. Mater.* **1996**, *8* (11), 928–932.
(16) Douglas, T.; Stark, V. T. *Inorg. Chem.* **2000**, *39* (8), 1828–1830.
(17) Uchida, M.; Flenniken, M. L.; Allen, M.; Willits, D. A.; Crowley, B. E.; Brumfield, S.; Willis, A. F.; Jackiw, L.; Jutila, M.; Young, M. J.; Douglas, T. *J. Am. Chem. Soc.* **2006**, *128* (51), 16626–33.
(18) Klem, M. T.; Mosolf, J.; Young, M.; Douglas, T. *Inorg. Chem.* **2008**, *47* (7), 2237–2239.
(19) Klem, M. T.; Young, M.; Douglas, T. *J. Mater. Chem.* **2010**, *20* (1), 65–67.
(20) Uchida, M.; Willits, D. A.; Muller, K.; Willis, A. F.; Jackiw, L.; Jutila, M.; Young, M. J.; Porter, A. E.; Douglas, T. *Adv. Mater.* **2009**, *21* (4), 458–462.
(21) Klem, M. T.; Suci, P.; Britt, D. W.; Young, M.; Douglas, T. *J. Adhes.* **2009**, *85* (2−3), 69–77.
(22) Kang, S.; Suci, P. A.; Broomell, C. C.; Iwahori, K.; Kobayashi, M.; Yamashita, I.; Young, M.; Douglas, T. *Nano Lett.* **2009**, *9* (6), 2360–2366.
(23) Broomell, C. C.; Birkedal, H.; Oliveira, C. L. P.; Pedersen, J. S.; Gertenbach, J. A.; Young, M.; Douglas, T. *Soft Matter* **2010**, *6* (14), 3167–3171.
(24) Jolley, C. C.; Uchida, M.; Reichhardt, C.; Harrington, R.; Kang, S.; Klem, M. T.; Parise, J. B.; Douglas, D. *Chem. Mater.* **2010**, *22* (16), 4612–4618.
(25) Michel, F. M.; Ehm, L.; Antao, S. M.; Lee, P. L.; Chupas, P. J.; Liu, G.; Strongin, D. R.; Schoonen, M. A. A.; Phillips, B. L.; Parise, J. B. *Science* **2007**, *316* (5832), 1726–1729.
(26) Cornell, R. M.; Schwertmann, U. *The iron oxides: structure, properties, reactions, occurrences, and uses*, 2nd ed.; Wiley-VCH: Weinheim, Germany, 2003; p 664.
(27) Dey, A.; Bomans, P. H. H.; Muller, F. A.; Will, J.; Frederik, P. M.; de With, G.; Sommerdijk, N. A. J. M. *Nat. Mater.* **2010**, *9* (12), 1010–1014.
(28) Gebauer, D.; Volkel, A.; Colfen, H. *Science* **2008**, *322* (5909), 1819–1822.

(29) Pouget, E. M.; Bomans, P. H. H.; Goos, J. A. C. M.; Frederik, P. M.; de With, G.; Sommerdijk, N. A. J. M. *Science* **2009**, *323* (5920), 1455–1458.
(30) Casey, W. H.; Swaddle, T. W. *Rev. Geophys.* **2003**, *41* (2), 1008.
(31) Jolley, C. C.; Douglas, T. *Biophys. J.* **2010**, *99* (10), 3385–3393.
(32) Lai, J. R.; Shafi, K. V. P. M.; Ulman, A.; Loos, K.; Yang, N. L.; Cui, M. H.; Vogt, T.; Estournes, S.; Locke, D. C. *J. Phys. Chem. B* **2004**, *108* (39), 14876–14883.
(33) Misra, R. D. K.; Gubbala, S.; Kale, A.; Egelhoff, W. F. *Mater. Sci. Eng., B* **2004**, *111* (2−3), 164–174.
(34) Chen, Q.; Zhang, Z. J. *Appl. Phys. Lett.* **1998**, *73* (21), 3156–3158.
(35) Yuan, J. K.; Li, W. N.; Gomez, S.; Suib, S. L. *J. Am. Chem. Soc.* **2005**, *127* (41), 14184–14185.
(36) Uchida, M.; Terashima, M.; Cunningham, C. H.; Suzuki, Y.; Willits, D. A.; Willis, A. F.; Yang, P. C.; Tsao, P. S.; McConnell, M. V.; Young, M. J.; Douglas, T. *Magn. Reson. Med.* **2008**, *60* (5), 1073–81.
(37) Pool, V.; Klem, M.; Jolley, C.; Arenholz, E. A.; Douglas, T.; Young, M.; Idzerda, Y. U. *J. Appl. Phys.* **2010**, *107* (9), 09B517.
(38) Chen, C. T.; Sette, F.; Ma, Y.; Modesti, S. *Phys. Rev. B* **1990**, *42* (11), 7262–7265.
(39) Hammersley, A. P.; Svensson, S. O.; Hanfland, M.; Fitch, A. N.; Hausermann, D. *High Pressure Res.* **1996**, *14* (4−6), 235–248.
(40) Qiu, X.; Thompson, J. W.; Billinge, S. J. L. *J. Appl. Crystallogr.* **2004**, *37* (4), 678.
(41) Chichagov, A. V.; Varlamov, D. A.; Dilanyan, R. A.; Dokina, T. N.; Drozhzhina, N. A.; Samokhvalova, O. L.; Ushakovskaya, T. V. *Crystallogr. Rep.* **2001**, *46* (5), 876–879.
(42) Farrow, C. L.; Juhas, P.; Liu, J. W.; Bryndin, D.; Bozin, E. S.; Bloch, J.; Proffen, T.; Billinge, S. J. L. *J. Phys.: Condens. Matter* **2007**, *19*, 335219.
(43) Lei, M.; de Graff, A. M. R.; Thorpe, M. F.; Wells, S. A.; Sartbaeva, A. *Phys. Rev. B* **2009**, *80*, 024118.
(44) Ammar, S.; Jouini, N.; Fiévet, F.; Stephan, O.; Marhic, C.; Richard, M.; Villain, F.; Moulin, C. C. D.; Brice, S.; Sainctavit, P. *J. Non-Cryst. Solids* **2004**, *345−46*, 658–662.
(45) Petkov, V.; Ren, Y.; Saratovsky, I.; Pasten, P.; Gurr, S. J.; Hayward, M. A.; Poeppelmeier, K. R.; Gaillard, J. F. *ACS Nano* **2009**, *3* (2), 441–445.
(46) Schedin, F.; Hill, E. W.; van der Laan, G.; Thornton, G. *J. Appl. Phys.* **2004**, *96* (2), 1165–1169.
(47) Brice-Profeta, S.; Arrio, M. A.; Tronc, E.; Letard, I.; Moulin, C. C. D.; Sainctavit, P. *Phys. Scr.* **2005**, *T115*, 626–628.
(48) Kang, J. S.; Kim, G.; Lee, H. J.; Kim, D. H.; Kim, H. S.; Shim, J. H.; Lee, S.; Lee, H.; Kim, J. Y.; Kim, B. H.; Min, B. I. *Phys. Rev. B* **2008**, *77*, 035121.
(49) Parker, M. J.; Allen, M. A.; Ramsay, B.; Klem, M. T.; Young, M.; Douglas, T. *Chem. Mater.* **2008**, *20* (4), 1541–1547.